

Tokamak MHD equilibria with reversed magnetic shear and sheared flow ¹

G. Poulipoulis^{†2}, G. N. Throumoulopoulos^{†3}, H. Tasso^{★4}

[†]*University of Ioannina, Association Euratom - Hellenic Republic,
Section of Theoretical Physics, GR 451 10 Ioannina, Greece*

[★]*Max-Planck-Institut für Plasmaphysik, Euratom Association,
D-85748 Garching, Germany*

Abstract

Analytic solutions of the magnetohydrodynamic equilibrium equations for a cylindrically symmetric magnetically confined plasma with reversed magnetic shear, $s < 0$, and sheared flow are constructed by prescribing the safety factor-, poloidal velocity- and axial velocity- profiles consistently with experimental ones. On the basis of the solutions obtained in most of the cases considered it turns out that an increase of $|s|$ and of the velocity components result in larger absolute values for the radial electric field, E_r , its shear, $|dE_r/dr| \equiv |E'_r|$, and the $\mathbf{E} \times \mathbf{B}$ velocity shear, $\omega_{\mathbf{E} \times \mathbf{B}} = |d/dr(\mathbf{E} \times \mathbf{B}/B^2)|$, which may play a role in the formation of Internal Transport Barriers (ITBs) in tokamaks. In particular for a constant axial magnetic field, $\omega_{\mathbf{E} \times \mathbf{B}}$ at the point where $E'_r = 0$ is proportional to $1 - s$. Also, $|E'_r|$ and $\omega_{\mathbf{E} \times \mathbf{B}}$ increase as the velocity shear takes larger values. The results clearly indicate that $s < 0$ and sheared flow act synergetically in the formation of ITBs with the impact of the flow, in particular the poloidal one, being stronger than that of $s < 0$.

¹A preliminary version of the present study was presented in the 29th EPS Conference on Plasma Phys. and Control. Fusion, Montreux, 17-21 June 2002 [1]

²me00584@cc.uoi.gr

³gthroum@cc.uoi.gr

⁴het@ipp.mpg.de

1. Introduction

Understanding Internal Transport Barriers (ITBs) in plasmas is very important for the advanced tokamak scenarios [2],[3]. The ITBs usually are associated with reversed magnetic shear profiles [4],[5] and their main characteristics are steep pressure profiles in the barrier region [6] and radial electric fields associated with sheared flows [7], [8]. The mechanism responsible for the formation of ITBs is far from completely understood. It is believed that the flow, the radial electric field, its shear and the $\mathbf{E} \times \mathbf{B}$ velocity shear,

$$\omega_{\mathbf{E} \times \mathbf{B}} = \left| \frac{d}{dr} \frac{\mathbf{E} \times \mathbf{B}}{B^2} \right|, \quad (1)$$

play a role in the barrier formation by mode decorrelation thus resulting in a reduction of the outward particle and energy transport [3], [9], [10].

The experimental evidence up to date has not made clear whether the reversed magnetic shear, $s < 0$, or the sheared flow (toroidal or poloidal) are more important for the ITBs formation. In some experiments the safety factor profile is considered as the crucial quantity (e.g. [11]) while according to others the necessity of reversed magnetic shear is questionable (e.g. [9]). On the other hand, the flow-either toroidal [12] or poloidal [13],[14] may be important in the formation of ITBs. Also, it has been argued that the toroidal velocity may be more important than the poloidal one (see for example Ref. [13]). It should be noted, however, that only few direct measurements of the poloidal velocity have been performed; this velocity is usually calculated by means of neoclassical theory [12].

The aim of the present work is to contribute to the answer of the above mentioned open questions by studying magnetohydrodynamic (MHD) cylindrical equilibria with reversed magnetic shear and sheared flow. The study can be viewed as an extension of a previous one on tokamak equilibria with incompressible sheared flows and monotonically increasing q -profiles in connection with certain characteristics of the L-H transition [15]. The work is conducted through the following steps: The profiles of certain free quantities, including the safety factor and the velocity components are first prescribed and then exact equilibrium solutions are constructed self consistently. This is the subject of Sec. 2. In Sec. 3 on the basis of the solutions obtained the equilibrium properties are examined and the impact of $s < 0$ and the flow on E_r , E'_r and $\omega_{\mathbf{E} \times \mathbf{B}}$ is evaluated. The conclusions are summarized in Sec. 4.

2. Cylindrical equilibria with reversed magnetic shear

The equilibrium of a cylindrical plasma with flow satisfies (in convenient units) the relation

$$\frac{d}{dr} \left(P + \frac{B_\theta^2 + B_z^2}{2} \right) + (1 - M_\theta^2) \frac{B_\theta^2}{r} = 0 \quad (2)$$

stemming from the radial component of the force-balance equation $\rho(\mathbf{v} \cdot \nabla)\mathbf{v} = \mathbf{j} \times \mathbf{B} - \nabla P$ with the aid of Ampère's law. Here, P is the plasma pressure; B_θ and B_z are the poloidal and axial components of the magnetic field, respectively; $M_\theta^2 = (v_\theta^2 \rho)/B_\theta^2$ is the square of the Mach number defined as the ratio of the poloidal velocity to the poloidal-magnetic-field Alfvén velocity. Because of the symmetry any equilibrium quantity depends only on the radial distance r and the axial velocity v_z as well as the velocity shear do not appear

in (2); also, the flow is incompressible. In addition to v_z four out of the five quantities in (2) can be prescribed.

On account of typical experimental ITB profiles we prescribed the quantities q , B_z , v_θ , v_z and ϱ as follows:
strongly reversed shear profile (SRS) (Fig. 1)

$$q(\rho) = q_c \left(1 - \frac{3\Delta q}{q_c} \frac{r_0^2}{r_{\min}^2} \rho^2 + \frac{2\Delta q}{q_c} \frac{r_0^3}{r_{\min}^3} \rho^3 \right) \quad (3)$$

or alternatively weakly reversed shear profile (WRS)

$$q(\rho) = q_c \left(1 - \frac{2\Delta q}{q_c} \frac{r_0}{r_{\min}} \rho + \frac{\Delta q}{q_c} \frac{r_0^2}{r_{\min}^2} \rho^2 \right) \quad (4)$$

where $\rho = r/R_0$ with r_0 defining the plasma surface, $q_c = q(r = 0)$, r_{\min} is the position of minimum q , and $\Delta q = q_c - q_{\min}$. The SRS-profile (3) does exhibit a maximum at the plasma center $r = 0$ in addition to the minimum one at $r = r_{\min}$ and has stronger magnetic shear in the central region just inside the q_{\min} position than that of the WRS one. It should be clarified, however, that the WRS profile (4), which does not have an extremum on the magnetic axis $r = 0$, has been chosen in order to simplify the calculations though the physical situation may not be well represented in the immediate vicinity of the magnetic axis;

$$B_z = B_{z0} [1 + \delta(1 - \rho^2)]^{1/2} \quad (5)$$

where B_{z0} is the vacuum magnetic field and the parameter δ is related to the magnetic properties of the plasma, i.e. for $\delta < 0$ the plasma is diamagnetic;
Gaussian-like poloidal velocity profile

$$v_\theta = 4v_{\theta0}\rho(1 - \rho) \exp \left[-\frac{(\rho - \rho_{\min})^2}{h} \right] \quad (6)$$

where the parameter h determines its broadness and $v_{\theta0}$ is the maximum of v_θ ; either peaked axial velocity profile

$$v_z = v_{z0}(1 - \rho^3)^3 \quad (7)$$

or Gaussian-like v_z profile similar to that of (6); and the density profile

$$\varrho = \varrho_0(1 - \rho^3)^3. \quad (8)$$

The following quantities can then be calculated: the poloidal magnetic field $B_\theta = \epsilon \rho B_z / q$ where $\epsilon = r_0/R_0$ is the inverse aspect ratio with $2\pi R_0$ associated with the length of the plasma column; the magnetic shear $s = (r/q)(dq/dr)$; the current density via Ampere's law; the electric field via Ohm's law; its shear E'_r and $\omega_{\mathbf{E} \times \mathbf{B}}$ by (1). Also, integration of (2) so that $P(r = r_0) = 0$ yields the pressure. The calculations have been performed analytically by developing a programme for symbolic computations [16] in connection with Ref. [17]. This also allowed us to examine conveniently purely poloidal flows, purely axial flows, z -pinch configurations or θ -pinch configurations as particular cases. The analytic expressions which can be derived readily by the programme are generally lengthy and will not be given explicitly here. Some concise and instructive expressions will only be presented in the next section along with typical profiles for the calculated quantities supporting the results obtained.

3. Results

We have set the following values for some of the parameters: $B_{z0} = 1$ Tesla, $\varrho_0 = 8.35 \times 10^{-8} \text{kg/m}^3$ corresponding to $n_0 = 5 \times 10^{19}$ particles/ m^3 , $\rho_{\min} = 0.5$, $\epsilon = r_0/R_0 \approx 1/3$, $\delta = -0.0975$, $q_{\min} = 2$, $\max v_\theta = 1 \times 10^4$ m/sec and $\max v_z = 1 \times 10^5$ m/sec; Consequently, it is guaranteed that $M_\theta^2 \approx M_z^2$, where $M_z^2 = (v_z^2 \varrho)/B_z^2$, a scaling typical in tokamaks because $B_z \approx 10 B_\theta$ and $v_z \approx 10 v_\theta$. It is noted here that since in tokamaks $M_\theta < 0.1$ the flow term in (2) is perturbative around the “static” equilibrium $M_\theta = 0$. Also, the choice $q_{\min} = 2$ was made because according to experimental evidence for $q_{\min} < 2$ strong MHD activity destroys confinement possibly due to a double tearing mode [18]. A similar result was found numerically for one-dimensional cylindrical equilibria with hollow currents in Ref. [19]. The impact of the magnetic shear and flow on the equilibrium, in particular on the quantities E_r , E'_r and $\omega_{\mathbf{E} \times \mathbf{B}}$, was examined by varying the parameters q_c , Δq , h , v_{z0} , and $v_{\theta 0}$ [Eqs. (3), (4), (6) and (7)].

For reversed magnetic shear profiles we came to the following conclusions:

1. Pressure

Substitution of B_θ and its derivative in terms of q and s in (2) yields

$$P' = -B_z B'_z \left[1 + \left(\epsilon \frac{r_0}{R_0} \right)^2 \right] + r_0 \rho [M_\theta^2 + (s - 2)] \left(\frac{B_z}{R_0 q} \right)^2. \quad (9)$$

For $s < 0$, increase of $|s|$ makes the pressure profile steeper (see also Fig. 2). Equation (9) also implies that the pressure profile becomes steeper when the plasma is more diamagnetic, i.e. when B'_z related to the parameter δ in (5) takes larger values.

2. Current density

- The axial current density profile becomes hollow and, irrespective of the reversal of the magnetic shear, there is a critical distance ρ_{cr} outside the q_{\min} position at which J_z becomes negative (Fig. 3). In particular, for $B_z = B_{z0} = \text{const.}$ one obtains

$$J_z = \frac{1}{r} \frac{d}{dr} (r B_\theta) = \frac{B_{z0}}{R_0 q} (2 - s) \quad (10)$$

Consequently, for $s > 2$, J_z reverses. The radial distances at which $J_z = 0$ for the SRS [Eq. (3)] and the WRS [Eq. (4)] q -profiles, respectively, are

$$\rho_{cr}^{SRS} = \rho_{\min} \left(\frac{q_c}{\Delta q} \right)^{1/3}$$

and

$$\rho_{cr}^{WRS} = \rho_{\min} \frac{q_c}{\Delta q}.$$

Therefore, the position of ρ_{cr} is shifted towards the center as s takes lower negative values. It is noted here that equilibrium toroidal current density reversal for monotonically increasing q -profiles was reported in Ref. [20] (Fig. 3 therein).

- Very large values of Δq on the order of 10^2 result in the formation of j_z profiles with "holes" in the central region- $j_z \approx 0$ - inside the ρ_{\min} position as demonstrated in Fig. 4, a result consistent with experimental evidence ([21], [22]).
- The total axial current $I_z = 2\pi r_0 B_\theta(r_0)$ for SRS profiles is smaller than that for WRS profiles.

3. E_r and E'_r

- Typical E_r profiles exhibit an extremum in the region around q_{\min} and vanish at $\rho = 0$ and $\rho = 1$ in agreement with experimental ones [7], [23]. Profiles with more than one extrema are also possible in the case of peaked v_z profiles, localized v_θ ones and $v_z v_\theta > 0$ as demonstrated in Fig. 5. Experimental profiles of this kind were reported in Ref. [23] (Fig. (9) therein).
- The main contribution to E_r comes from the velocity, to which is proportional, and particularly from the poloidal one (Fig. 6).
- E_r is sensitive to the relative orientation of v_z , v_θ and B_z ; in particular, for $v_z v_\theta < 0$ $|E_r|$ is larger than that for $v_z v_\theta > 0$. (Fig. 7). Similar results hold for E'_r (Fig. 8) and $\omega_{\mathbf{E} \times \mathbf{B}}$.
- For extended velocity profiles with $v_z \neq 0$, an increase of $|s|$ results in an increase of $|E_r|$ (Fig. 9), $|E'_r|$ and $\omega_{\mathbf{E} \times \mathbf{B}}$. If $v_z = 0$, however, $|s|$ has no impact on $|E_r|$ and $|E'_r|$, as can be seen by inspection of $\mathbf{E} = \mathbf{v} \times \mathbf{B}$, and very weak impact on $\omega_{\mathbf{E} \times \mathbf{B}}$. This result indicates that the presence of v_z "activates" the impact of s on E_r , E'_r and $\omega_{\mathbf{E} \times \mathbf{B}}$.
- An increase of the velocity shear nearly does not affect or even decreases the maximum $|E_r|$ (Fig. 10) but increases $|E'_r|$ (Fig. 11).

4. $\omega_{\mathbf{E} \times \mathbf{B}}$

- A typical profile of $\omega_{\mathbf{E} \times \mathbf{B}}$ has two large local maxima at the positions where the edges of the barrier are expected to be located in addition to other two smaller local ones (Fig. 12). In most of the cases considered the maximum in the $s < 0$ region is slightly larger than that in the $s > 0$ region. (see Fig. 12). In particular, for $B_z = \text{const.}$ at the point where $E'_r = 0$ one obtains:

$$\omega_{\mathbf{E} \times \mathbf{B}} = \left| \frac{(1-s) \left(\epsilon \frac{\rho v_z}{q} - v_\theta \right)}{R_0 q \left[1 + \left(\epsilon \frac{\rho}{q} \right)^2 \right]} \right| \quad (11)$$

Eq. (11) implies the following:

1. $\omega_{\mathbf{E} \times \mathbf{B}}$ depends on the relative sign of v_z , v_θ and B_z , a result which we confirmed by $\omega_{\mathbf{E} \times \mathbf{B}}$ profiles obtained via the symbolic computation programme.
2. The factor $(1-s)$ indicates that $\omega_{\mathbf{E} \times \mathbf{B}}$ for nearly shearless stellarator equilibria may be lower than that for tokamak equilibria with $s < 0$.

3. Despite the scaling $v_z \approx 10v_\theta$, for tokamak pertinent parametric values the contributions of v_z -in connection with the term $\epsilon\rho v_z/q$ - and v_θ to $\omega_{\mathbf{E} \times \mathbf{B}}$ are of the same order of magnitude, a result indicating the importance of the poloidal velocity.
- For extended velocities (large values of the parameter h or/and peaked v_z - profile) a percentage increase of $|s|$ in the barrier region results:
 1. in approximately the same percentage increase of $\omega_{\mathbf{E} \times \mathbf{B}}$ if the velocity is purely axial (Fig. 13).
 2. nearly does not affect the value of $\omega_{\mathbf{E} \times \mathbf{B}}$ if $v_\theta \neq 0$.
 - An increase of the flow shear (variation of the parameter h from 0.1 to 0.001) causes a mean percentage increase of $\omega_{\mathbf{E} \times \mathbf{B}}$ as large as 0.7 of that of the flow shear. (Fig. 14).
 - The impact of a variation of the v_θ -shear on $\omega_{\mathbf{E} \times \mathbf{B}}$ is stronger than of the same variation of the v_z -shear.
 - The maximum increase of $\omega_{\mathbf{E} \times \mathbf{B}}$ is caused by v_θ in the case of non-vanishing peaked v_z profiles.
 - Inspection of $\mathbf{v}_{\mathbf{E} \times \mathbf{B}} = \mathbf{E} \times \mathbf{B}/B^2$ and (1) implies that $\omega_{\mathbf{E} \times \mathbf{B}}$ for a z-pinch is equal to that for an equilibrium with purely axial flow. The same equality is valid for a θ -pinch in comparison with an equilibrium with purely poloidal flow. In addition, it holds that

$$\omega_{\mathbf{E} \times \mathbf{B}-\text{z-pinch}} \approx 10\omega_{\mathbf{E} \times \mathbf{B}-\theta\text{-pinch}}. \quad (12)$$

4. Conclusions

The self consistent study of cylindrical equilibria with reversed magnetic shear and sheared flow presented in the previous sections led to the following conclusions:

1. For reversed magnetic shear profiles ($s < 0$):
 - The larger values of $|s|$ the steeper the pressure profile.
 - The axial current density profile become hollow.
 - Strong reversed shear profiles formed by appropriately large values of Δq are associated with "hole" axial current density profiles.

These results are consistent with experimental ones.

2. Irrespective of the sign of s the axial current density can reverse in the outer plasma region, the reversal point being shifted towards the plasma core as s takes lower negative values.
3. An increase of either $|s|$ or the velocity results generally in an increase of $|E_r|$, $|E'_r|$ and $\omega_{\mathbf{E} \times \mathbf{B}}$.
4. An increase of the velocity shear results in an increase of $|E'_r|$ and $\omega_{\mathbf{E} \times \mathbf{B}}$.

5. For a given value of $|s|$, $\omega_{\mathbf{E} \times \mathbf{B}}$ takes slightly larger values in the $s < 0$ region than in the $s > 0$ region.
6. E_r , E'_r and $\omega_{\mathbf{E} \times \mathbf{B}}$ are sensitive to the relative orientation of v_θ , v_z and B_z . In particular, they take larger values for $v_z v_\theta < 0$ rather than for $v_z v_\theta > 0$.
7. The presence of v_z activates $s < 0$, in the sense that for $v_z = 0$, E_r and E'_r are s -independent. Also, for $v_z = 0$, $s < 0$ has very weak impact on $\omega_{\mathbf{E} \times \mathbf{B}}$.
8. The impact of the poloidal flow and its shear on E_r , E'_r and $\omega_{\mathbf{E} \times \mathbf{B}}$ is stronger than that of the axial flow and the magnetic shear.

Presuming that E_r , E'_r and $\omega_{\mathbf{E} \times \mathbf{B}}$ are of relevance to the ITBs formation, the above results clearly indicate that the reversed magnetic shear and the sheared flow have synergistic effects on this formation with the flow, in particular the poloidal one, and its shear playing an important role.

References

- [1] Poulipoulis G. , Throumoulopoulos G.N. , Tasso H. (2002) Proceedings of the 29th EPS Conference on Plasma Phys. and Control. Fusion. Montreux Switzerland 17-21 June 2002, ECA Vol. 26B, P-4.076
- [2] Hazeltine R.D. and S.C. Prager S.C. (2002) Physics Today **55** 30
- [3] Sakamoto Y. *et al* (2001) Nucl. Fusion **41** 865
- [4] Strait E.J. *et al* (1995) Phys. Rev. Lett. **75** 4421
- [5] Conway G.D. *et al* (1998) Plasma Phys. Control. Fusion **43** 1239
- [6] Levinton F.M. *et al* (1995) Phys. Rev. Lett. **75** 4417
- [7] Tala T.J.J. *et al* (1998) Plasma Phys. Control. Fusion **43** 507
- [8] Candy R. and Waltz R.E. (2003) Phys. Rev. Lett. **91** 045001
- [9] Burrell K.H. *et al* (1998) Plasma Phys. Control. Fusion **40** 1585
- [10] Terry P.W. (2002) Rev. Mod. Phys. **72** 109
- [11] Eriksson L.-G. *et al* (2001) Phys. Rev. Lett. **88** 145001
- [12] Crisanti F. *et al* (2001) Nuclear Fusion **41** 883
- [13] Bell R.E. *et al* (1998) Phys. Rev. Lett. **7** 1429
- [14] Rice J.E. *et al* (2001) Nucl. Fusion **41** 277
- [15] Siminztis Ch. , Throumoulopoulos G.N. , Pantis G. , Tasso H. (2001) Phys. Plasmas **8** 2641
- [16] A typical version of the programme is available at the cite <http://users.uoi.gr/me00584/plasma.htm>. Further information can be requested to the first author (G.P.)
- [17] Wolfram Research, Mathematica, version 4.1
- [18] Wolf R.C. *et al* (2000) Phys. Plasmas **7** 1839
- [19] Kerner W. and Tasso H. (1982) Plasma Physics **24** 97
- [20] Mashke E.K. (1973) Plasma Phys. **15** 535
- [21] Fujita T. *et al* (2001) Phys. Rev. Lett. **87** 245001
- [22] Hawkes N.C. *et al* (2002) Plasma Phys. Control. Fusion **44** 1105
- [23] Meister H. *et al* (2001) Nucl. Fusion **41** 1633

Figure captions

Fig. 1: SRS and WRS safety factor profiles associated with Eqs. (3) and (4), respectively. It is noted that the finite slope of the WRS curve at $\rho = 0$ may not represent well the physical situation in the immediate vicinity of the magnetic axis.

Fig. 2: WRS pressure profiles for $\Delta q = 4$ and $\Delta q = 14$.

Fig. 3: Toroidal current density profiles for $\Delta q = 4$. It is noted that the finite slope of the WRS curve at $\rho = 0$ may not represent well the physical situation in the immediate vicinity of the magnetic axis.

Fig. 4: Toroidal current density profile for WRS, $q_c = 102$ and $\Delta q = 100$ that demonstrates the current "hole" in the core region.

Fig. 5: Electric field profile for WRS with v_z peaked and v_θ localized having three local extrema.

Fig. 6: Two E_r -profiles the one with $v_z = 0$ and the other with $v_\theta = 0$ for SRS and Gaussian-like velocity profiles. E_r is normalized with respect to its value at $\rho = 0.5$ for $v_z = 0$.

Fig. 7: Two E_r -profiles for v_z peaked and SRS, the one with $v_\theta \cdot v_z > 0$ and the other with $v_\theta \cdot v_z < 0$. The profiles are normalized with respect to the first case at $\rho = 0.5$.

Fig. 8: Two profiles of E'_r with v_z peaked and SRS, the one with $v_\theta \cdot v_z > 0$ and the other with $v_\theta \cdot v_z < 0$. The profiles are normalized with respect to the first case at $\rho = 0.3$.

Fig. 9: Profiles of E_r with peaked axial and extended poloidal velocities for WRS and two different values of Δq . The profiles are normalized with respect to the case with $\Delta q = 4$ at $\rho = 0.5$.

Fig. 10: Profiles of E_r with $v_z = 0$ for SRS and either extended ($h = 0.1$) or localized ($h = 0.001$) poloidal velocity. The profiles are normalized with respect to the first case at $\rho = 0.5$.

Fig. 11: Two profiles of E'_r for SRS with $v_z = 0$ the one for extended ($h = 0.1$) and the other for localized ($h = 0.001$) poloidal velocities. The profiles are normalized with respect to the second case at $\rho = 0.55$.

Fig. 12: Typical $\omega_{\mathbf{E} \times \mathbf{B}}$ -profile for WRS, peaked axial and localized poloidal velocities.

Fig. 13: Profiles of $\omega_{\mathbf{E} \times \mathbf{B}}$ for WRS, peaked axial velocity, and either $\Delta q = 4$ or $\Delta q = 14$. The profiles are normalized with respect to the first case at $\rho = 0.45$.

Fig. 14: $\omega_{\mathbf{E} \times \mathbf{B}}$ -profile for SRS, Gaussian-like axial and poloidal velocity components both either extended ($h = 0.1$) or localized ($h = 0.001$). The profiles are normalized with respect to the first case at $\rho = 0.3$.

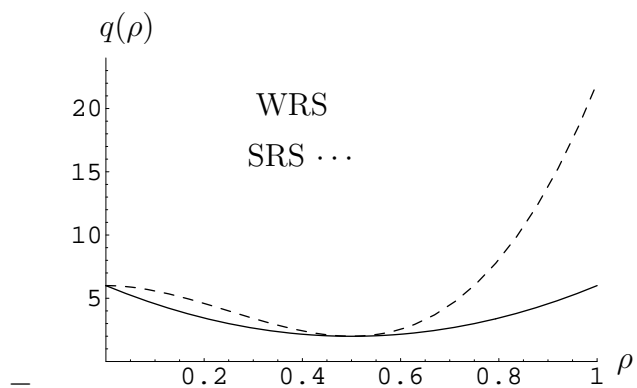


Figure 1:

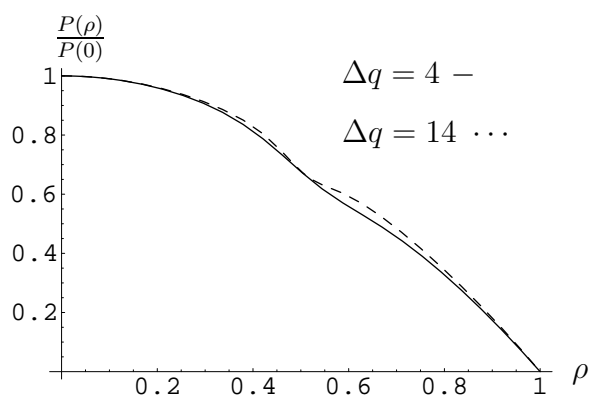


Figure 2:

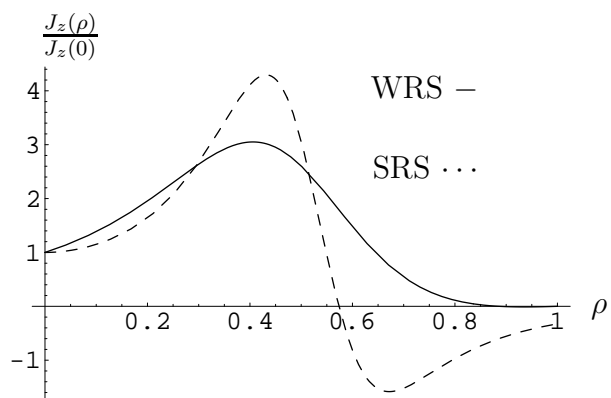


Figure 3:

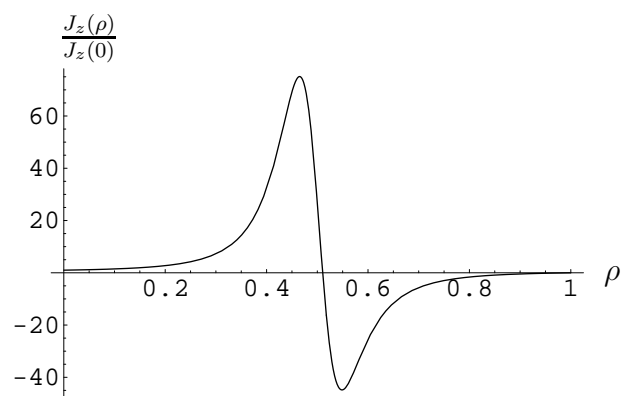


Figure 4:

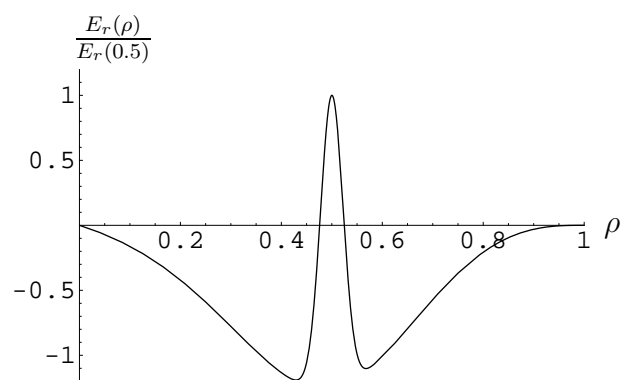


Figure 5:

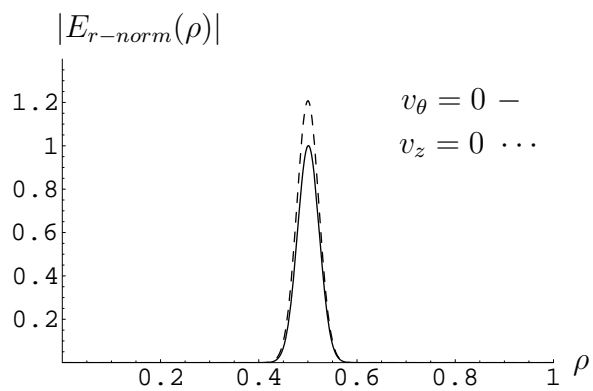


Figure 6:

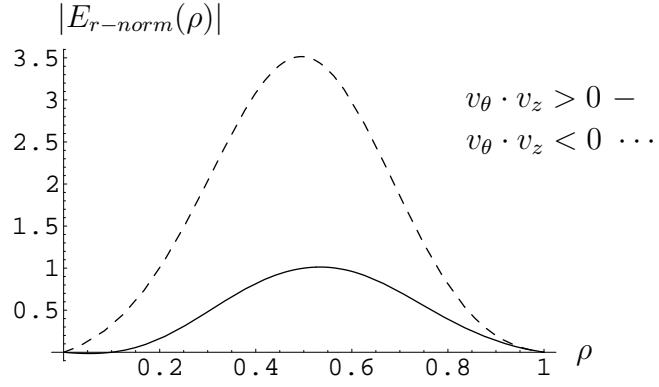


Figure 7:

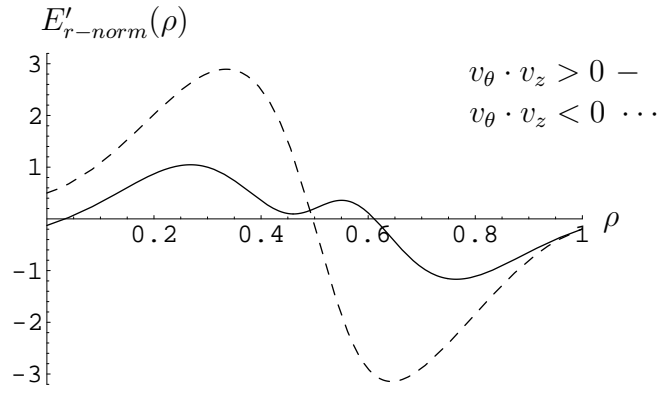


Figure 8:

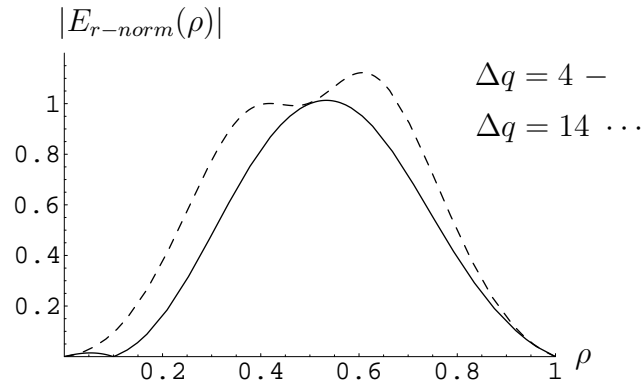


Figure 9:

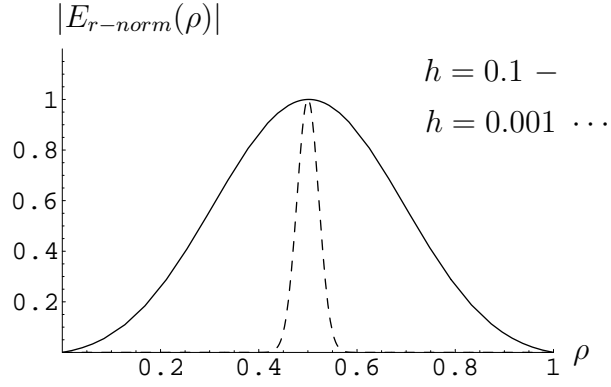


Figure 10:

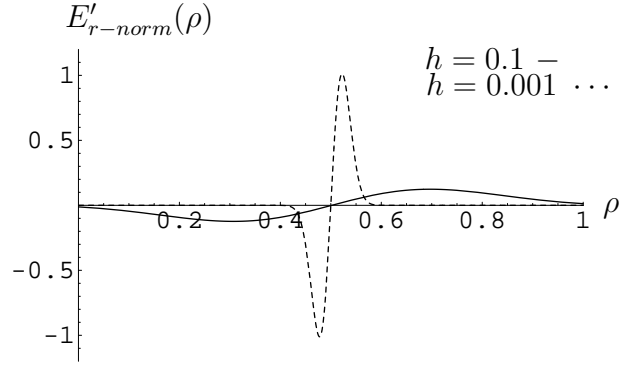


Figure 11:

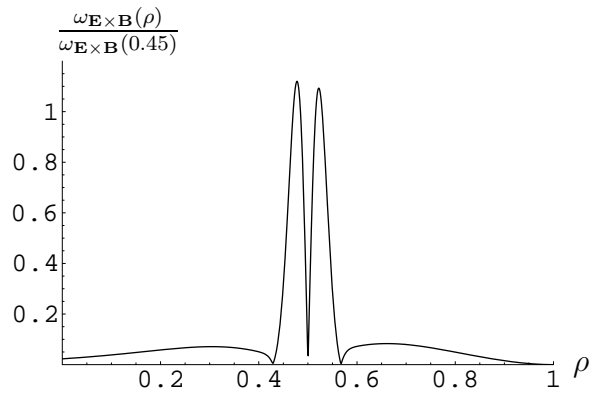


Figure 12:

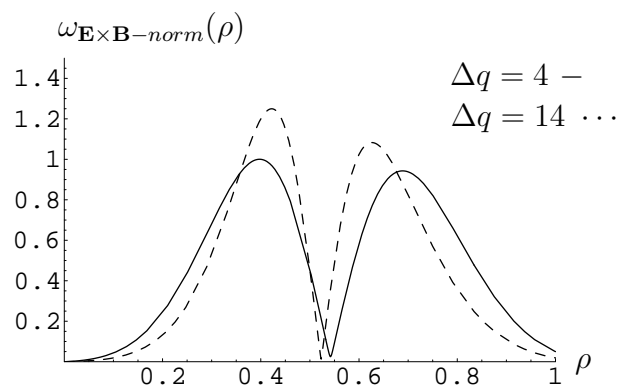


Figure 13:

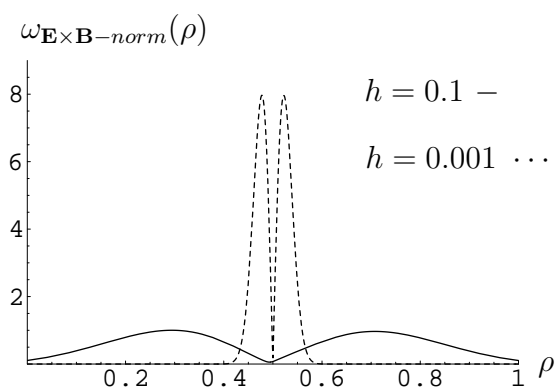


Figure 14: